Ionization and stopping of heavy ions in dense laser-ablated plasmas

C. Couillaud, R. Deicas, Ph. Nardin, M. A. Beuve, J. M. Guihaumé, and M. Renaud
Commissariat à l'Énergie Atomique, Service de Physique et Techniques Nucléaires, Centre d'Etude de Bruyères-le-Chatel, F-91680 Bruyères-le-Châtel, France

M. Cukier, C. Deutsch, and G. Maynard
Laboratoire de Physique des Gaz et des Plasmas, Bâtiment 212, Université Paris XI, 91405 Orsay Cedex, France
(Received 17 August 1993)

Enhanced plasma stopping and enhanced projectile ionization in plasma are considered within the framework of the standard stopping model (SSM), the most economical extension to plasmas of the standard cold-matter formalism. The main goal of this work is to check quantitatively the SSM predictions using the setup SPQR1 (stopping plasma quantitatively reinforced) developed at Bruyères-le-Chatel. It consists of a laser-ablated C or Al plasma synchronized with a 50-MeV Cu ion beam bunched out of a tandem Van de Graaff accelerator. A combination of a Thomson parabola spectrometer and an ionographic tube provides charge-state distribution and energy-loss data. Plasma expansion is modeled and yields electron-temperature and density-profile-matching diagnostics performed in the interaction chamber. In agreement with theoretical expectations, charge-distribution maxima at the plasma exit are shifted toward higher ionization compared to the equivalent results in cold matter. The distribution width is smaller than its cold-target homologue. Energy losses in partially ionized C and Al targets are several times larger than in the respective cold solid. The relevance to heavy-ion-driven inertial fusion is emphasized.

PACS number(s): 52.40.Mj, 52.70.−m, 52.80.−s, 28.52.−s

I. INTRODUCTION

The interaction of energetic heavy-ion beams with dense plasma targets is a topic of central importance for asserting the feasibility of inertial confinement fusion (ICF) through intense beams of charged particles [1–4]. In this area, a lot of significant effort has already been devoted to the experimental verification of enhanced stopping capabilities exhibited by free electrons in fully ionized hydrogen targets displayed in linear accelerator beam lines [5–7]. For this purpose, energetic and partially stripped ions ($0.6 \leq E/A \leq 6$ MeV) of nearly all kinds have already been used. Simultaneously, similar results were obtained with intense deuterium beams igniting plastic targets, through pulsed power systems [2].

In this way, it is possible to validate theoretical predictions of the so-called standard stopping model (SSM) [5], the most economical extension to hot matter of the Bohr-Bethe-Bloch (3B) high projectile velocity formalism for ion stopping in cold matter. The corresponding stopping power reads as

$$-\frac{dE}{dx}=\frac{4\pi N_0 e^4 \rho}{A_T m_e V_I^2} Z_{\text{eff}}^2(V_1)[\bar{Z}\ln\Lambda_F+(Z_T-\bar{Z})\ln\Lambda_B]\ , \tag{1.1}$$

where $E=MV_1^2/2$, ρ is the density of the stopping medium, N_0 is Avogadro's number, e is the electron charge, m_e is the electron mass, Z_{eff} is the effective charge of beam ions, V_1 is the projectile velocity, A_T is the target atomic weight, Z_T is the target atomic number, $\bar{Z}$ is the average ionization in the target, and Λ_B,Λ_F are the arguments of the Coulomb logarithms for bound and free electrons, respectively.

For high target-electron velocities, Λ_B is given by the familiar Bethe expression

$$\Lambda_B=\frac{2m_e v_1^2}{I_{\text{av}}}\ , \tag{1.2}$$

where I_{av} is the Bethe mean excitation energy [3]. The expression for Λ_F is

$$\Lambda_F=\frac{2m_e v_1^2}{\hbar\omega_p}\ , \tag{1.3}$$

where ω_p is the plasma frequency. At low velocity, when one has $\Lambda_F<1$, it must be modified.

Equation (1.1) implies the neglect of any collective stopping effect due to the high intensity of the ion beam, in agreement with recent investigations of the target corona instabilities [8]. Equation (1.1) is the high-temperature limit of more sophisticated estimates for the bound- and free-electron stopping power in the dense target plasma. Moreover, for partially stripped projectiles, an equally significant enhanced stopping also arises from the strongly reduced recombination [9] between incoming ion and free electrons. Such a drastic behavior maintains a relatively high Z_{eff}, in contrast to that in cold matter, where the ion projectile can easily pick up bound electrons from target atoms (or ions), located near its trajectory. Thus the enhanced-plasma-stopping (EPS) physical content rests essentially on the much enhanced response of plasma free electrons, together with highly increased Z_{eff} values compared to nominally equivalent cold tar-

gets, i.e., ones with the same line-integrated nuclear density (number/cm^2). n_e is the free-electron nuclear density target and l the linear ion range within.

In a recent work, we have already compared the quantitative SSM prediction with stopping-power measurements performed on light ions in the 1 MeV/amu energy range. For this purpose, we made use of a plasma column with fully ionized hydrogen (or deuterium) inserted on the beam line of a linear tandem accelerator. The projectile effective charge $Z_{\rm eff}(V_1)$ has been then purposefully taken either as negligible (fully ionized, He-like structure, etc.) or followed numerically through a code described in Sec. II. This procedure has then allowed us to determine quantitatively the EPS featured by terms within brackets in the right-hand side in Eq. (1.1).

In contradistinction to that effort, the main goal of the present work is to investigate thoroughly the impact of plasma target conditions (n_e,T_e) on the overall important prefactor $Z_{\rm eff}(V_1)$. As far as theoretical and numerical expectations are concerned, the most conspicuous feature is the enhanced projectile ionization in plasma (EPIP) compared to projectile ionization in a neutral, or less ionized target with the same electron linear density (fluence). This effect is based on an argument going back to Bell [9], according to which it appears much more unlikely for the incoming projectile to pick up electrons from free-electron plane waves than from bound orbitals on target ions. The respective rates are likely to differ by three orders of magnitude.

Broadly speaking, the present work is devoted to a confirmation of the EPS in nonhydrogenic targets, and to a thorough examination of the various facets of the EPIP in the same conditions. The ion projectile is essentially 50 MeV Cu^{9+}.

The basic theoretical features of EPS and EPIP are reviewed in Sec. II. An adequate model allowing the predictions of (n_e,T_e) diagnostics for the laser-ablated plasma is developed according to ideas provided by Afanas'ev *et al.* [14] and Kidder [15] in Sec. II and in the appendixes. The stopping-plasma-quantitatively-reinforced (SPQR1) setup designed for the synchronized interaction of a bunch Cu ion beam with the expanding plasma is presented in Sec. IV. The required ion-beam spectrometry and synchronization principles are discussed in Sec. V.

Cu-ion charge-state distributions at the plasma exit are presented and discussed at length in Sec. VI. The corresponding average losses are displayed in Sec. VII. Results and discussions are summarized in Sec. VIII.

II. STANDARD STOPPING MODEL

The enhanced projectile effective charge, as well as the enhanced plasma stopping have already been amply documented theoretically and numerically for hydrogen plasmas. Here, we intend to specify those features for nonhydrogenic plasma targets retaining a significant fraction of bound electrons. First, we briefly recall the general trends of the standard stopping model (SSM), already worked out previously, and focus attention on the average ion energy loss and projectile charge distribution at the plasma exit. In this work, we mostly consider the Cu^{9+}-ion beam with pulse length $\tau_f=50$ nsec, intensity $I_f=10$ nA. So, the average interion distance $do\sim 550$ μm remains much larger than the electron screening length λ_D of ablated plasma with typical parameters $T_e\sim 100$ eV and $n_e\sim 10^{19}$ cm^{-3}, i.e., $\lambda_D\sim 0.0235$ μm. In nearly every situation of practical interest, one has $\lambda_D \ll do$. Therefore, one can safely reduce the beam-target interaction to that of one single ion.

A. Enhanced plasma stopping

Simulation of ion-beam scattering in the plasma target shows that Coulomb diffusion is rather weak, so the ion projectile taken as a pointlike charge experiences a nearly linear trajectory in the stopping medium. In these conditions, the ion plasma stopping may be expressed as a linear superposition,

$$-\frac{dE}{dx}=\sum_i \alpha_i+\sum_i \beta_i+\gamma \ , \tag{2.1}$$

where γ is the free-electrons contribution; β_i, the contribution of bound electrons on target ion i; and α_i, the contribution of target ion i.

Usually $\alpha_i \ll \beta_i$ or γ. Therefore one can safely restrict oneself to the electron stopping expression (1.1) in the high-temperature limit of present concern. Then, one gets a very important scaling law,

$$\frac{\Delta E}{E}\approx\frac{n_e l}{E^2} \ , \tag{2.2}$$

in terms of the average linear electron density (fluence) in target. l denotes the linear projection of the ion range on the initial direction at the target entrance. Equation (2.2) is in agreement with the obvious fact that for $E/A\in$[1 MeV/amu, 1 GeV/amu], the prefactor $A=4\pi e^4 Z_{\rm eff}^2(V_1)/m_e v_1^2$ is the dominant one in the SSM stopping expression (1.1). In order to highlight the various contributions to electron stopping it seems appropriate to explain Eq. (2.1) under the form

$$-\frac{dE}{dx}=An_T Z_T L \ , \tag{2.3}$$

in terms of target atom density n_T (atomic number Z_T). In the plasma target, the stopping number reads as

$$L=\frac{\bar{Z}}{Z_T}L_f+\frac{(Z_T-\bar{Z})}{Z_t}L_b+\frac{Z_{\rm eff}V_0}{V_1}L_1 + \left[\frac{Z_{\rm eff}V_0}{V_1}\right]^2 f\left[\frac{Z_{\rm eff}V_0^2}{V_1^2}\right] \ . \tag{2.4}$$

L_f and L_b pertain respectively to free- and bound-electron contributions. $\bar{Z}$ is the average target ionization, v_0 is the Bohr velocity (=1 a.u.). L_1 features the so-called Barkas effect

$$L_1=\frac{3E_i}{\hbar m_e v_1^3}\frac{e^2}{4\pi\epsilon_0}\log_{10}\left[\frac{2m_e v_1^2}{\bar{I}}\right] \ , \tag{2.5}$$

with E_i, the average energy of the plasma ion, and $\bar{I}$, the

potential of mean excitation for bound electrons. The last one is a Bloch contribution where

$$f\left[\frac{Z_{\text{eff}}^2 V_0^2}{V_1^2}\right]=-\sum_{k=1}^{\infty}\frac{1}{k\left[k^2+\left[\frac{Z_{\text{eff}}V_0}{V_1}\right]^2\right]}, \quad (2.6)$$

The contributions (2.5) and (2.6) are rather weak compared to the first two. For a 50-MeV Cu^{9+}-ion beam, the Bloch term reduces to

$$\frac{Z_{\text{eff}}^2 V_0^2}{V_1^2} f\left[\frac{Z_{\text{eff}}^2 V_0^2}{V_1^2}\right]=-1.1 ,$$

while for an Al plasma target with $\bar{Z}=6$, one gets

$$E_i=241.4 \text{ eV}, \quad \bar{I}=457.5 \text{ eV}, \quad L_1=1.8 .$$

Therefore, one sees that Barkas and Bloch cancel each other to a large extent. We are thus essentially left with the first two terms. Integrating the stopping power over the projectile ion range and taking averages over projectile charge states, one obtain the average energy loss

$$[\overline{\Delta E} \text{ (MeV)}]=302.4\times 10^{-24}\overline{Z_{\text{eff}}^2}[L_f \overline{n_{el}} + (Z_T-\bar{Z})L_b \overline{n_{il}}] , \quad (2.7)$$

with $\overline{n_i l}\,(\text{cm}^{-2})=\overline{n_e l}(\text{cm}^{-2})/\bar{Z}$, which is a quantity well adapted to the SPQR1 experimental device detailed below.

B. Enhanced projectile ionization in plasma

1. *Basic mechanisms*

The instantaneous projectile charge $Z_{\text{eff}}(V_1)$ is the result of a balance [10] between various two-body processes detailed below. First, we consider the one-electron excitation of projectile ions colliding with target free electrons and ions (denoted by A), respectively:

$$\begin{aligned} &X^{q+}+e\rightarrow X^{q+*}+e' , \\ &X^{q+}+A^{p+}(E)\rightarrow X^{q+*}+A^{P+}(E') . \end{aligned} \quad (2.8)$$

Those two processes are only significant for a deexcitation time long compared to intercollision time. Similarly, ionization through collisions with target free electrons and ions given as

$$\begin{aligned} &X^{q+}+e\rightarrow X^{(q+1)+}+2e , \\ &X^{q+}+A_j^{p+}\rightarrow X^{(q+1)+}+A_j^{(p-1)+} , \\ &X^{q+}+A_j^{p+}\rightarrow X^{(q+1)+}+A_j^{p+}+e , \end{aligned} \quad (2.9)$$

feature the most important contribution to projectile ionization. α_{ie} refers to the electron reaction rate averaged over electron distribution and α_{ij} denotes a similar quantity for the sum of the following ion processes. Autoionization matters when the projectile ion is doubly excited, with one electron ionized and the other one falling into a lower level.

Radiative recombination

$$X^{q+}+e\rightarrow (X^{(q-1)+})+h\nu \quad (2.10)$$

has to be taken into account for highly ionized targets. α_{RR} is the corresponding reaction rate averaged over free-electron distribution. Dielectronic recombination

$$X^{q+}+e\rightarrow (X^{(q-1)+})^{**}\rightarrow X^{(q-1)+}+h\nu \quad (2.11)$$

is given for its reaction rate a constant average value $\alpha_{\text{DR}}=10^{-11}\text{ cm}^3\text{ s}^{-1}$.

This value has been formerly proposed as an upper bound some time ago by Nardi and Zinamon [9]. More recent investigations by Chen [9] show that α_{DR} is also significantly dependent on the target temperature.

However, the reported variations remain moderate, especially for a projectile ionization smaller than 10. Nevertheless, in order to estimate the final impact of those variations in the projectile charge, we have performed a parameter study which shows that increasing α_{DR} by an order of magnitude or reducing it by the same amount does not change at all the results displayed in Figs. 1–3 as well as in the experimental situations encountered below. This remarkable stability is due to the fact that in a partially ionized plasma target, the projectile charge balance essentially arises from ionizing collisions and also charge transfer from bound electrons to the target ions. Other free-electron contributions such as dielectronic recombination or three-body recombination

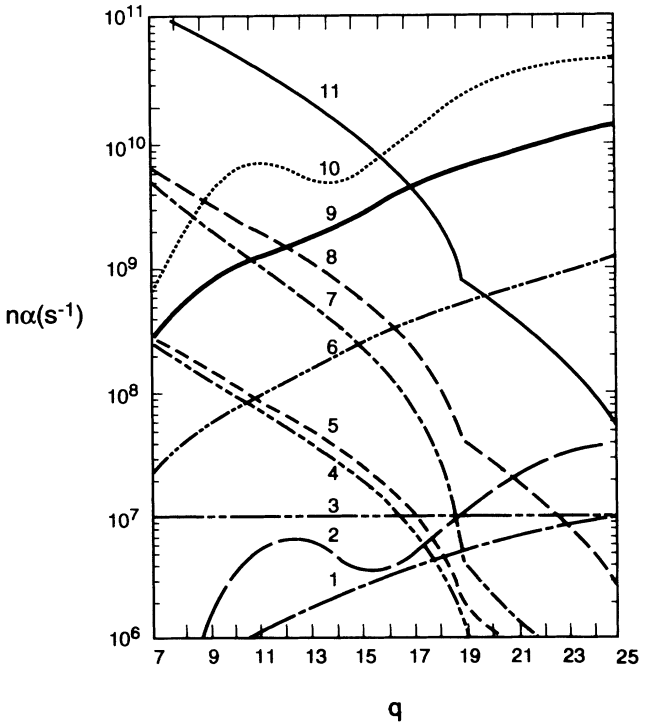

FIG. 1. Reaction rates (sec^{-1}) weighted by density of excited target bound states, versus charge state q, encountered in the interaction of 50-MeV Cu ions with an Al plasma ($T_e=250$ eV, $n_e=10^{18}\text{ cm}^{-3}$). Curve labeling: 1, $n_e\alpha_{\text{RR}}$; 2, $n(12+)\alpha_{qq-1}$; 3, $n_e\alpha_{\text{DR}}$; 4, $n(12+)\alpha_{ij}$; 5, $n(9+)\alpha_{ij}$; 6, $n(9+)\alpha_{qq-1}$; 7, $n_e\alpha_{ie}$; 8, $n(10+)\alpha_{ij}$; 9, $n(10+)\alpha_{qq-1}$; 10, $n(11+)\alpha_{qq-1}$; 11, $n(11+)\alpha_{ij}$.

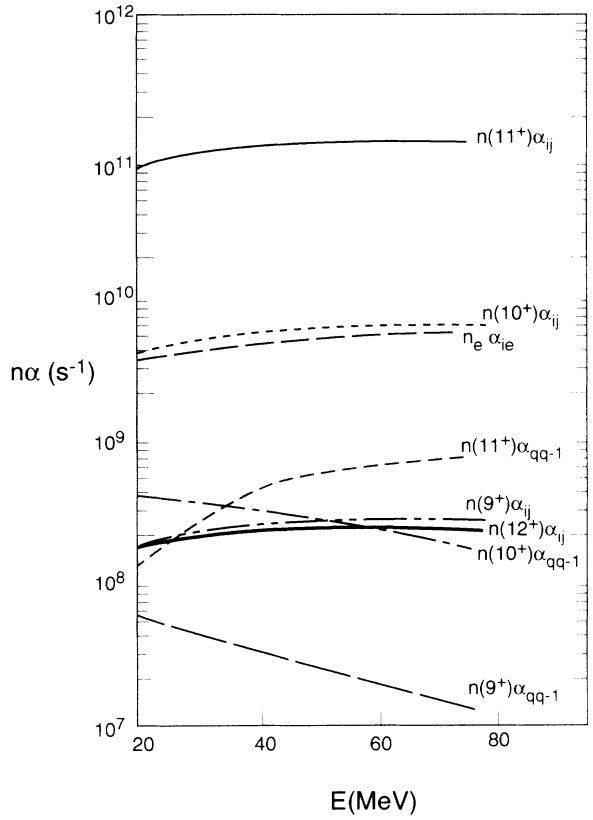

FIG. 2. Reaction rates in the interaction of the 50-MeV Cu^{7+} ion with the Al plasma of Fig. 1 in terms of projectile energy. Other unspecified quantities are as in Fig. 1.

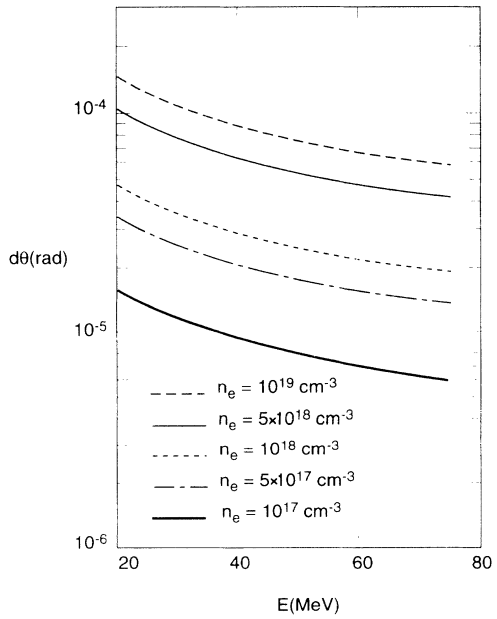

FIG. 3. Scattering angle $d\theta$ experienced by the 50-MeV Cu^{9+} ion in terms of projectile energy in an Al plasma with $T_e=250$ eV, $10^{17}\leq n_e$ (cm^{-3}) $\leq 10^{19}$ for an inflight time $\sim 10^{-12}$ s.

remain three orders of magnitude below the charge transfer as soon as there is 0.5% of bound electrons in the target.

Charge transfer

$$X^{q+}+A^{p+}\rightarrow X^{(q-1)+}+A^{(p+1)+}\ , \tag{2.12}$$

with the rate α_{qq-1} is the most important recombination process in neutral gases, solids, or partially ionized plasmas. However, in a fully ionized medium, this contribution nearly vanishes. Such a behavior readily accounts for a drastic reduction of recombination in plasma. As a result, projectile charge is expected to stay at the same plateau value over most of its velocity range. Nevertheless, charge-transfer recombination is so long that it is dominant even in the presence of only a few target bound orbitals.

Decay by spontaneous emission

$$X^{q+}(E)\rightarrow X^{q+}(E')+h\nu$$

appears non-negligible for highly excited projectiles. Finally, three-body recombination is ruled out because at high projectile velocity and average electron density, conservation of impulse cancels three-body reactions. More specifically, momenta of the two recombining electrons have to compensate one another at the ion location. Such an occurrence decreases very rapidly with increasing projectile velocity, as clearly evidenced by a calculation due to Bailey, Lee, and More [9].

As already hinted above, charge transfer is the most efficient capture process, so one expects a higher projectile charge in a fully ionized plasma than in the equivalent cold gas. Also, for a partially ionized plasma with a large number of bound electrons, one expects that the projectile equilibrium charge, reached when electron losses balance gains, is obtained at higher projectile velocity that in totally stripped plasmas.

In Fig. 1, we picture the above considered reaction rates versus charge state q for the 50-MeV Cu ions interacting with a strongly ionized Al plasma, where $T_e=250$ eV and $n_e=10^{18}$ cm^{-3}. The Al plasma is assumed to be in a coronal regime with Al^{n+} ions and $n=9-12$.

Except for dielectronic recombination, which remains q independent, all other processes are strongly affected by the varying projectile charge state. On the other hand, when the projectile charge state (see Fig. 2) is kept fixed, the corresponding rates stay nearly constant in terms of incoming kinetic energy. It is also instructive to confirm the aforementioned assumption of there being no deflection through strong Coulomb collision of ion projectiles with target ions. Scattering angles experienced by Cu^{9+} ions at various energies, in a strongly ionized Al plasma, are shown to stay below 10^{-4} rad (Fig. 3).

2. *Numerical simulations*

Now we turn to the elaboration of Monte Carlo code based on the above analysis and data for stopping and projectile charge states. We wish to track its evolution while flowing in the plasma target. Its results will be compared to experimental measurements presented

below.

Taking the laser-ablating beam parallel to the y direction, the expanding plasma shows the electron-density profile

$$n_e(x,y,z)=n_{e0}\exp\left[\frac{-y}{L_y}\right]\exp\left[\frac{-(x^2+z^2)}{R^2}\right].$$

L_y and R respectively denote gradient lengths for n_e along y and along $r=(x^2+z^2)^{1/2}$.

Plasma temperature varies only along the laser axis with $T_e=T_i$. Projectiles are tracked within a Cartesian frame with their origin at the plasma center. A packet of N_f ions is treated as N_f times an isolated ion interacting with the plasma. Projectile ions are supposed to remain in their ground state. The numerical code provides instantaneous energy loss as well as Coulomb diffusion within a cone of maximum aperture.

Every ion evolution is treated statistically through a Monte Calo algorithm, at the plasma entrance, and after each collision, as well. Electron gain or loss is considered stochastically through the above detailed reaction rates. The time elapsed between two collisions is treated similarly with respect to the average relaxation rate. The diffusion angle is averaged over several interactions.

Ion charge computed at every trajectory step is fixed by the last gain or loss process, selected out by random sampling over probabilities associated with various reactions. At a given point, where projectile ion charge is q, one can determine [11] an electron-loss probability

$$p_+=\frac{\left[n_e\alpha_{ij}+\sum_j n_j\alpha_{ij}(j)\right]\left[1-\exp\left[-t\Big/\left(\tau_e+\sum_j\tau_j\right)\right]\right]}{\tau_e+\sum_j\tau_j}, \tag{2.13}$$

an electron-gain probability

$$p_+=\frac{\left[n_e(\alpha_{\rm RR}+\alpha_{\rm DR}+\sum_j n_j\alpha_{qq-1}(j)\right]\left\{1-\exp\left[-t\Big/\left[\tau_e+\sum_j\tau_j\right]\right]\right\}}{\tau_e+\sum_j\tau_j}, \tag{2.14}$$

in terms of

$$\begin{aligned}\tau_e&=n_e(\alpha_{ie}+\alpha_{\rm RR}+\alpha_{\rm DR}),\\ \tau_j&=n_j(\alpha_{ij}(j)+\alpha_{qq-1}(j)),\end{aligned} \tag{2.15}$$

and a probability for no change of charge,

$$p_0=1-p_+-p_-. \tag{2.16}$$

One can also determine two branching ratios $p_1=p_+$ and $p_2=p_++p_-$, with $0\le p_1\le p_2\le 1$.

Then, one samples randomly a real number $h\in[0,1]$. If $h\le p_1$, one gets electron loss ($q\to q+1$) and a gain ($q\to q-1$) for $p_1\le h\le p_2$. For $p_2\le h$, there is no charge change ($q\to q$).

At every time step, one thus prescribes the instantaneous q value. At the plasma entrance, and also after each collision, the various reaction rates are computed. One can define an average relaxation time τ for electron gain or loss, together with collision probability $p=1-e^{-t/\tau_0}$. The time of occurrence of the succeeding collision is then obtained by random sampling between $\tau/10$ and 10τ. The ion trajectory is then integrated between two successive collisions through a calculation of stopping power and Coulomb diffusion.

Then the probability of each atomic reaction is computed, which yields the two branching ratios p_1 and p_2. In addition, one samples again a number between 0 and 1, which determines a given atomic process. Calculations are taken up further for new values of E, q, spatial coordinates, and velocity. Reaction rates are computed anew, and so on, up to the plasma exit. The code requires at least 1000 ions in order to minimize statistical fluctuations.

III. LASER-ABLATED PLASMA

In order to emulate realistically the driven-pellet interaction expected in ion-driven inertial fusion, we consider laser ablation of nonhydrogenic planar targets of low Z materials such as carbon and aluminum. Their low atomic number insures a large proportion of free electrons under laser irradiation. Therefore, we expect a large EPS and a large EPIP as well.

A. Laser

Typically, one envisions plasma parameters such as $1\le T_e$ (eV) ≤ 150 and $10^{17}\le n_e$ (cm^{-3}) $\le 10^{19}$. We make use of a CO_2 laser ($\lambda=10.6$ μm) delivering an irradiance $\sim 10^{11}$ W/cm^{-2}. The target is submitted to a 10^{-7} mbar vacuum. In order to synchronize the laser with the heavy-ion beam, one keeps to a minimum the mismatch between plasma production and the arrival of ion bunches. So, the laser discharge is ignited with a synchronous signal from the accelerator by another Nd:YAG laser, with weak time fluctuation. The considered setup can deliver a 20-J pulse with a 50-ns half-maximum duration.

B. Plasma production

The impact of laser light on the target provokes an immediate ionization, with a charge density decreasing from

the ablated surface. Plasma gets heated within a few picoseconds through inverse bremsstrahlung in a zone thickness comparable to a laser wavelength [12]. The kinetic pressure rises very rapidly, so the plasma starts expanding from the target spot with a velocity close to sound velocity.

Simultaneously, the plasma ablation produces through momentum conservation a compression wave preceded by a shock wave. The plasma absorbs light as long as its frequency ω_{pe} remains smaller than the laser frequency $\omega_{10.6\,\mu m}=1.78\times10^{14}$ rad/s^{-1}. So, the photons do not penetrate a plasma with $n_e \geq n_{ec}=10^{19}$ e cm^{-3}. When $\omega \geq \omega_{pe}(n_e \leq n_{ec})$, the laser wave propagates in plasma and gets attenuated. In an Al plasma with $T_e=100$ eV, $\bar{Z}=7$, the absorption coefficient is $K=2.3\times10.3$ m^{-1}. CO_2 laser light is then absorbed on a 430-μm thickness.

On the other hand, when $n_e > n_{ec}$, light gets specularly back reflected with a T_e-independent absorption coefficient

$$K=\frac{2\omega p_e}{c}=3.75\times10^{-6}n_e^{1/2}(\mathrm{cm}^{-3}) , \tag{3.1}$$

As far as the thermal state of the CO_2 created plasma is concerned it seems that it can be understood within a corona equilibrium approximation. T_e retains a meaning in the considered medium because the equilibration time τ_{ee} for the target electrons is much smaller than the heating time. For instance, for a 100-eV plasma with $n_e=10^{19}$ cm^{-3}, one gets $\tau_{ee}=5\times10^{-12}$ s, much smaller than the duration laser pulse $\tau_L=50$ ns.

Three-body recombination should remain much smaller than radiative recombination in an optically thin plasma. In order to simplify plasma diagnostics, one is particularly interested in a stationary regime. The density of plasma ions with charge Z then fulfills $dn_Z/dt=0$, so that

$$\frac{n_{Z+1}}{n_Z}=\frac{S(Z,\,T_e)}{\alpha(Z+1,\,T_e)} , \tag{3.2}$$

in terms of $S(T,\,T_e)$, the ionization coefficient and/or collision; and $\alpha(Z+1,\,T_e)$, the radiative recombination coefficient. The effective ionization time is given by the longest and last ionization, i.e.,

$$\tau_Z=\frac{1}{n_e[S(Z_{\max}-1\,,T_e)+\alpha(Z_{\max},T_e)]} , \tag{3.3}$$

which is close to the heating time when ionization and recombination equilibrate each other, so that

$$S(Z_{\max}-1\,,T_e)\cong\alpha(Z_{\max},T_e) , \tag{3.4}$$

which yields $\tau_Z\sim(n_eS)^{-1}$ and

$$\tau_Z(\mathrm{sec})=\frac{10^{12}}{n_e(\mathrm{cm}^{-3})} . \tag{3.5}$$

The stationary plasma assumption allows one to connect the target ion charge in the target to the electron temperature through [13] (Z_T=target atomic number)

$$\bar{Z}=26\left[\frac{[T_e\ (\mathrm{keV})]}{1+\left[\frac{26}{Z_T}\right]^2[T_e\ (\mathrm{keV})]}\right]^{1/2} . \tag{3.6}$$

C. Plasma expansion in vacuum

In view of the difficulties encountered in resolving the space-time dependence of density and temperature, there is an obvious interest in modeling economically the plasma expansion to obtain temperature and density gradients for the electron component. The plasma expansion has a characteristic time τ_L, the half-width of the laser pulse which brings in a characteristic density gradient length $L_p=c_S\tau_L$, in terms of c_S, the isothermal sound velocity in the plasma. The spatial extension and duration τ_f of ion bunches limits the modeling accuracy.

For $\tau_f \ll \tau_L$, the plasma looks stationary during the interaction. Similarly, for a beam diameter much less than L_p, n_e and T_e may be taken constant in the plane transverse to particle propagation. In the present experimental setup one has $\tau_f \cong 50$ ns, whereas the beam diameter $\sim$2 mm is much larger than the n_e gradient length in the plasma. So, there is no point is discussing in detail the space-time evolution of the plasma.

The present work therefore emphasizes less sophisticated but robust models. For this purpose,we derive temperature and density profiles from fluid mechanics equations. Even then, the treatment has to be further simplified, because it is not possible to sort out $n_e(\mathbf{r},t)$ and $T_e(\mathbf{r},t)$. This explains why we consider the laser-target interaction during the laser pulse, with a constant plasma flow. This procedure, due to Afanas'ev [14], yields t-independent n_e and T_e profiles. In the second step, the plasma is taken in a spherical expansion with a time dependence decoupled from the space one. Then stationary and t-dependent solutions are matched against each other. So, the stationary model is used as providing limit conditions to the t-dependent one. Technicalities and analytic results of the stationary modeling are then detailed in Appendix A. Time-dependent solutions are worked out in Appendix B.

D. Simulation

Expressions (B2) and (B3) for T_e and n_e profiles provide a radial evolution displayed in Fig. 4 at different times. The r dependence of T_e and n_e in Eqs. (B2) and (B3) is explained by assuming a plasma isothermal expansion. At the beginning, two distinct regions coexist with different temperatures T_l and R_h, respectively, given by

$$\left[T_{el}\ (\mathrm{eV})\right]=(2.8\pm0.2)\times10^{-2}[\phi_L^{1/3}\ (\mathrm{W/cm^2})] \tag{3.7a}$$

and

$$T_{eh}\ (\mathrm{eV})=(1.65\pm0.20)\times10^{-5}[\phi_L^{2/3}\ (\mathrm{W/cm^2})] , \tag{3.7b}$$

in terms of laser flux. Then, one takes the electron-density profile in the form

$$n_{eh}(r)=n_{eh}\exp(-r/L_h)\ ,$$
$$n_{el}(r)=n_{el}\exp(-r/L_l)\ , \tag{3.8}$$

unchanged under expansion, where L_h and L_l represent density gradient lengths. Then, n_{eh}, L_l, L_h, and L_l become t-dependent quantities prescribed by the above modeling which also determines their values at $t=\tau_L$.

The radial profiles given in Fig. 4 have been obtained for the initial conditions $\tau_L=50$ ns, $E_L=30$ J, $r_0=400$ μm, and $A=27$ (aluminum target), which allow us to compute T_e and n_e profiles in ranges $r\in[0,5$ mm] and $t\in[50,1000$ ns] through the parameters $\Phi_\Lambda=1.2\times10^{11}$ W/cm^{-2}, $T_{el}=138$ eV and $T_{eh}=400$ eV, $\overline{Z}=8$, $\overline{V^2}=29.5\times10^9$ m^{2}s^{-2} and $v_s^2=1.4\times10^9$ m^{2}s^{-2}, $T_s=57$ eV and $T_{cr}=114$ eV, $r_{cr}=2.2$ mm, $n_s=5.9\times10^{20}$ cm^{-3}, and $\gamma_0=2.8\times10^4$, required to operate the Afanas'ev formalism developed in Appendix A.

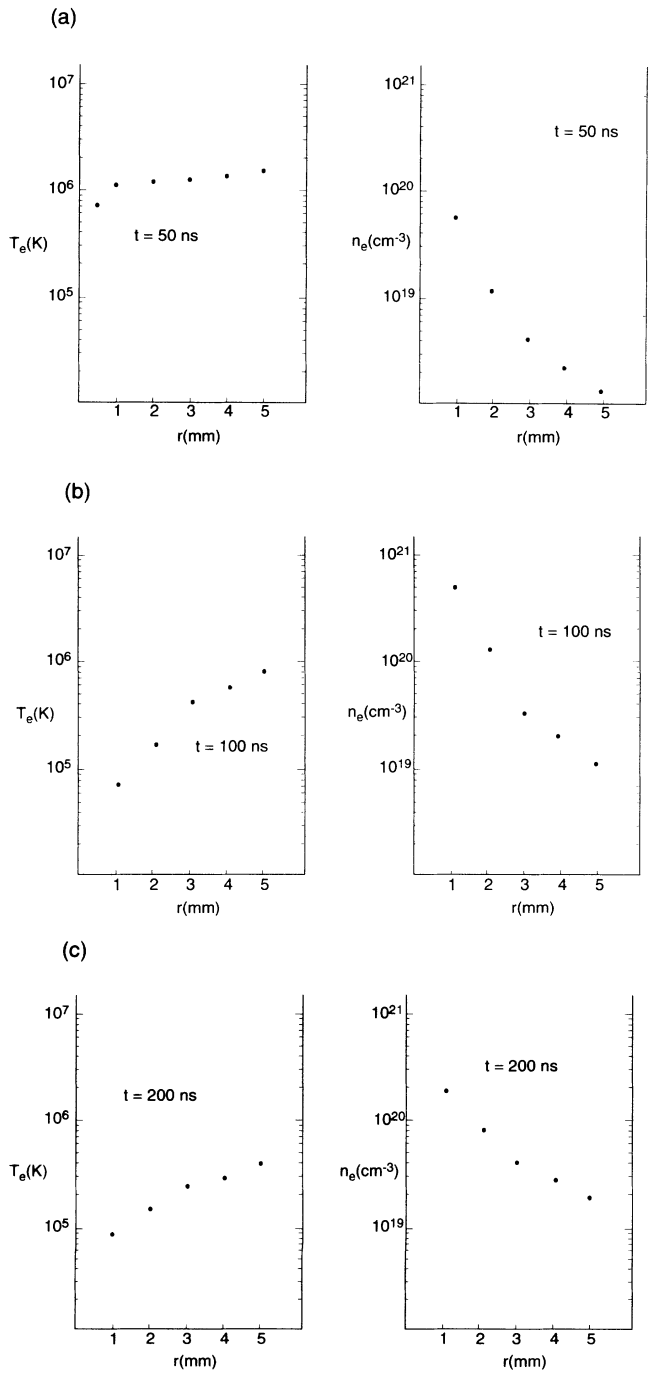

FIG. 4. Radial profiles for electron temperature and electron density derived from the Afanas'ev-Kidder model (Appendixes A and B): (a) $t=50$ ns, (b) $t=100$ ns; (c) $t=200$ ns.

E. $\overline{E_e}$ and $\overline{N_e}$

When the ion beam penetrates the expanding plasma (Fig. 5) it first encounters regions with increasing n_e up to the center [16]. Then, n_e decreases from the center up to the exit edge [17]. Beam particles are transversely distributed over a circular cross section, so each projectile ion is not affected by the same (n_e, T_e) parameters. Therefore, one has to take suitable averages for estimating stopping power and charge-state distribution.

The plasma radius corresponds to an ion density asymptotically equal to the neutral species density n_n in residual vacuum. For a residual pressure p at $T_0=300$ K, one has $n_n=2.69\times10^{19}\times(p/p_0)=6.7\times10^9$ cm^{-3} for $p=2\times10^{-7}$ mbar with $p_0=1015$ mbar.

We consider an ion beam with a 2-mm collimation diameter (see Fig. 5) which propagates parallel to the target (axis $0x$). The linear electron-density mean value is written

$$\overline{n_e l}=\frac{\int\int n_e(x,y,z)\,dy\,dz}{\int\int dy\,dz}\ , \tag{3.9}$$

where $n_e(x,y,z)$ denotes an instantaneous density profile. Integration has to be performed on a domain restricted by a beam envelope. Mean temperature $\overline{T_e}$ is computed in the same fashion. In a frame attached to the ion-beam center (x',y',z'), one has

$$x'=x,\quad y'=y-a\ ,\quad z'=z\ ,$$

so

$$\int\int\int dx\,dy\,dz = \int_0^{2a} dy \int_0^{\sqrt{a^2-(y-a)^2}} dx \int_0^{\sqrt{R_p^2-x^2-(y-a)^2}} dz$$

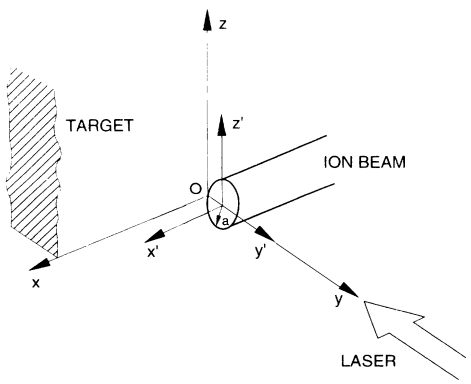

FIG. 5. Schematics of laser-target interaction.

with a equal to the beam radius and R_p equal to the plasma radius.

The expression in the right-hand side pertains to the plasma frame. A beam shifted 5 min up above the laser impact will get a y quadrature between 4 and 6 mm. Other quadratures remain unchanged.

IV. EXPERIMENTAL SETUP

A. Ion beam-plasma interaction

The theoretical arguments leading to the enhanced projectile ionization in plasma detailed above suggest a clear path to their experimental verification. Present day accelerators are not yet able to deliver enough of an intense ion beam to ignite cold matter into plasma. Therefore, one has to fire independently a synchronized target with the incoming ion beam.

This is the basic principle of the setup SPQR1 developed at Bruyères-Le-Chatel [4,16]. It is rather similar to the setup SPQR2 used at Orsay, making use of a synchronized plasma column. Another very important concept in this modeling is that the intrabeam ion-ion average distance remains much larger than the target-electron screening length. So, as far as enhanced plasma stopping is concerned, one is entitled to reduce the beam-plasma interaction to an isolated ion-plasma one. Our present goals are more ambitious. We intend to use the SPQR1 system to provide simultaneous measurements for checking out EPIP and EPS in nonhydrogenic and partially ionized targets.

The basic features of the ion beam-plasma interaction are very similar to those of the SPQR2 setup previously considered. For instance, beam energy loss ΔE has to be optimized against free-electron linear density (fluence) in the target according to [5] (l = linear ion path in target)

$$\frac{\Delta E}{E}=\frac{n_e l}{E^2} . \tag{4.1}$$

The main differences between SPQR2 and the SPQR1 system displayed here lie essentially in the very different time scales. In SPQR2, the plasma lifetime (100 μsec) is much longer than the ion-beam microstructure (2 nsec). In the present situation, those times are nearly equal and last 50 nsec.

It is not possible, with those conditions, to proceed to a well-resolved plasma diagnostics in the n_e and T_e of the target. We therefore rely on average target parameters $\overline{n_e}$ and $\overline{T_e}$.

B. Layout

The general layout [18] essentially consists (see Fig. 6) of a linear tandem 7-MV accelerator delivering Cu^{q+} ($5 \le q \le 9$) ions at 50 MeV (i.e., 0.793 meV/amu). The Cu-ion beam and the light of a CO_2 laser converge onto the same target plate. The interaction chamber is followed by a Thomson parabola spectrometer (TPS) providing charge-state and stopping-power measurements. Finally, an ionographic tube (IT) [11] yields imagery recording for the exiting ion projectiles. The ion beam is pulsed with a frequency $\nu_f = 2.5$ MHz at an intensity I_F. The number of ions N_f with charge q in a single bunch is therefore

$$N_f=\frac{I_f}{\nu_f q e}=\frac{2.5\times 10^{12} I_f(\text{nA})}{q} . \tag{4.2}$$

Typically, such a system delivers 2800 ions with $q=9$ at an intensity of 10 nA. The ion projectiles penetrate the target chamber (Fig. 7) through a calibrated hole in an alumina plate. This latter plate emits a visible light (white or pink) when directly impacted, which secures an easy spatial control of beam transport and also the spatial concidence of the ion beam with laser-ablated plasma. Ion projectile propagate in a vacuum better than 10^{-6} mbar. The target chamber is also subjected to a 10^{-7} mbar vacuum. It includes an x-ray spectrometer and an ion charge collector target plate mechanically movable with respect to the ion beam.

C. Plasma diagnostics

As already noted above, it is not possible to resolve, in time, density and temperature measurements. This ion charge collector permits the determination of an average $\overline{T_e}$. The T_e space-time dependence is derived from the

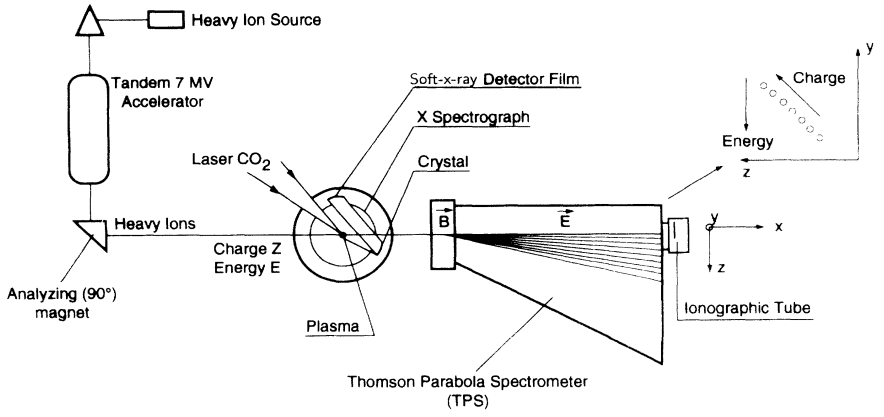

FIG. 6. General layout of the SPQR1 setup.

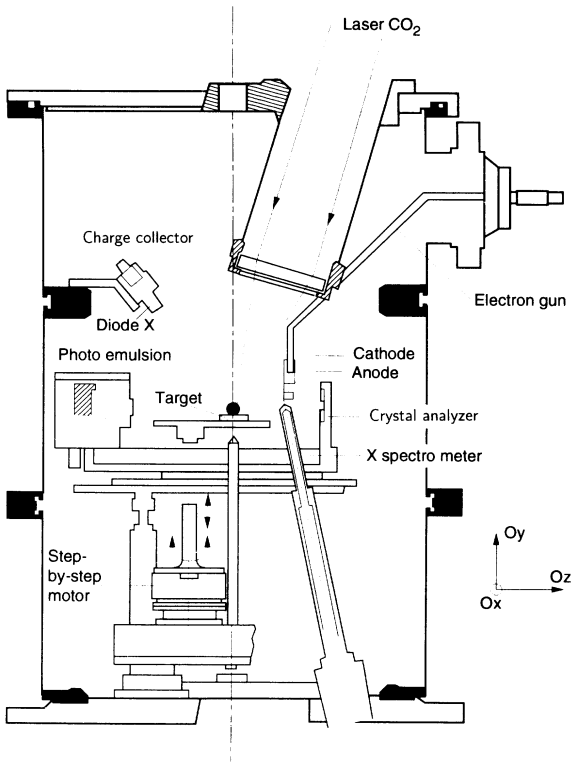

FIG. 7. Interaction chamber. The ion beam propagates along the x axis.

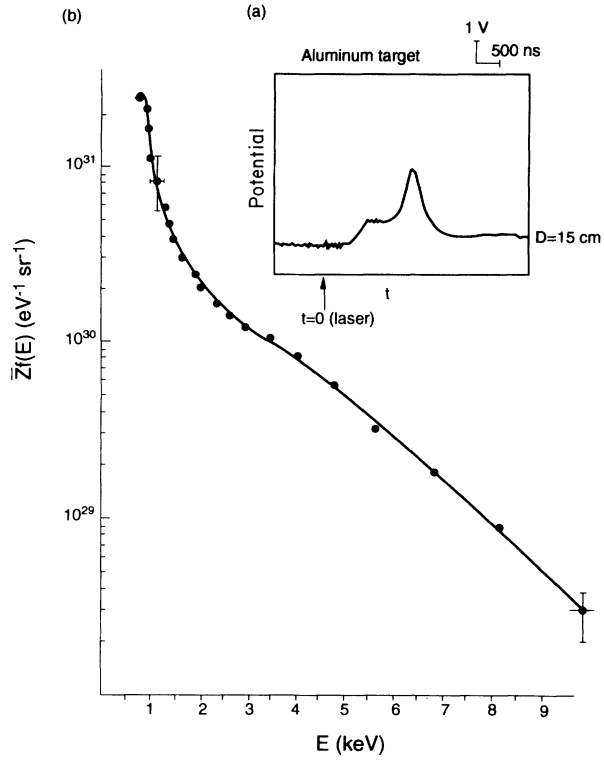

FIG. 8. (a) Charge collector signal polarized at -150 V. (b) Energy spectrum for collected Al ions from laser-ablated plasma.

expansion modeling worked out in Sec. III. Ion charge collector measurements and initial target irradiation conditions are then introduced as limit values in the Afanas'ev-Kidder modeling [14,15]. The calculated electron number density is dependent on the model. The plasma x-ray emission is calibrated with a Si $K\alpha$ spectrum.

D. Charges collector

The system shown in Fig. 8(a) is currently employed for the determination of the ion velocity distribution dN_i/dV_i in expanding plasmas. It measures the ion time of flight, i.e., the asymptotic ion velocity. In order to be significant, the measurement process should preserve the ion charge state. The recombination probability $W=n_0\sigma D$ is expressed in terms in terms of residual neutral gas atom density n_0, target-collector distance D, and electron-capture cross section σ ($\simeq 10^{-15}$ cm^2 for C^{6+}).

For an acceptable $W \leq 5\%$, residual pressure should be smaller than

$$P_{\text{lim}} = 3.8\times 10^{-17}\frac{W}{\sigma D} ,$$

i.e., $\leq 10^{-4}$ mbar for an expanding C^{6+} plasma located at $D=21$ cm from the target plate. Al has a higher recombination cross section, so $p \leq 10^{-7}$ mbar, in this case.

Two charge collectors and respectively located at 15 and 21 cm from the target, under a 40° observation angle relative to the target normal. Measured ion current $I_c(t)$ yields the energy spectrum $f(E)=dN_i/dE$ of plasma ions through ($\bar{Z}$ = average ion charge in plasma)

$$dN_i = \frac{I_c(t)}{\bar{Z}_e}dt , \tag{4.3}$$

where $\bar{Z}$ is taken constant during expansion. If D is sufficiently large to neglect the duration of plasma expansion, the ion (mass m_i) kinetic energy fulfills

$$d|E| = \frac{m_i D^2}{t^3}dt . \tag{4.4}$$

Combining Eqs. (4.3) and (4.4) provides

$$f(E) = \frac{I_c(t)t^3}{\bar{Z}em_iD^2} . \tag{4.5}$$

The low-energy and thermal component may be written as

$$f(E)dt = N_i\left[\frac{4}{\pi}\right]^{1/2}\left[\frac{1}{E_{\text{th}i}}\right]^{3/2} e^{-E/E_{\text{th}i}}\sqrt{E}\,dt . \tag{4.6}$$

In Fig. 8b, one has plotted $\bar{Z}f(E)E^{-1/2}$, in terms of E, for the thermal pat of the spectrum. The slope of the line yields T_e. The argument runs as follows. If one assumes that during expansion electrons yield all their energy to ions with equal initial temperatures ($T_e=T_i$), one gets $E_{\text{th}i}=2k_BT_e$. Charge collectors also allow us to determine average energy and mean quadratic velocity for plasma ions through

$$\bar{E}=\tfrac{1}{2}m_i\overline{V_i^2}=\tfrac{1}{2}m_iD^2\frac{\int_{t_1}^{t_2}\frac{I_c(t)dt}{t^2}}{\int_{t_1}^{t_2}I_c(t)dt} . \tag{4.7}$$

During adiabatic expansion, the quadratic mean velocity is related to adiabatic sound velocity through ($\gamma=\frac{5}{3}$)

$$\overline{V^2}=\left[\frac{\gamma+1}{\gamma-1}\right]\gamma c_S^2 , \tag{4.8}$$

in terms of sound isothermal velocity c_S fulfilling

$$c_S^2\ (m^2s^{-2})]\cong\frac{9.58\times10^7(\bar{Z}+1)[T_e\ (\text{eV})]}{A} ,$$

A being the target ion atomic mass.

V. ION-BEAM SPECTROMETRY AND SYNCHRONIZATION

A. Thomson parabola spectrometer (TPS)

Before plasma interaction, the ion packet is monoenergetic with a charge q. At the plasma exit, one observes a distribution of energy and charge states. To resolve the various components, one thus makes use of a Thomson parabola spectrometer (TPS) in the post-interaction region [Fig. 9(a)], where ions experience a double reflection in the parallel magnetic field **B** and electric field **E**, successively. **B** splits apart the various charges, whereas **E** resolves in energy the ion distribution. The TPS operates under a reduced pressure $\sim5\times10^{-7}$ mbar. It is located just after the interaction chamber, on the incident beam direction.

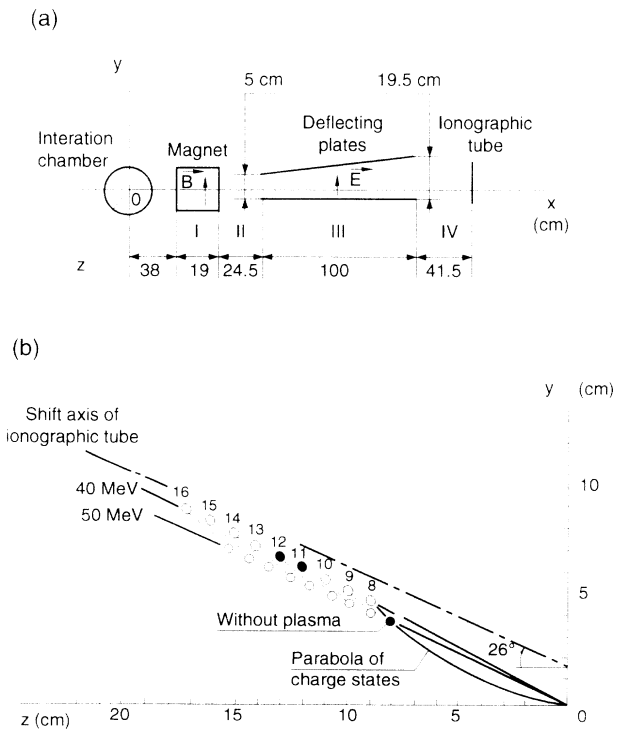

FIG. 9. (a) Schematics of the Thomson parabola spectrometer (TPS). (b) Traces of the analyzed ion beam at the TPS exit.

An ion beam with charge q, energy E, and mass $M=Am_p$ penetrates successively four regions. On the TPS analysis plane, the ion impact is defined by

$$Y=\alpha\frac{qV}{MV^2} , \quad Z=\beta\frac{qB}{MV^2} , \tag{5.1}$$

with constants α and β. U denotes the electric potential between plates. Equations (5.1) show that ions with the same q/M are located on the same parabola branch [Fig. 9(b)]. Ions with the same velocity are located on a straight line out of the origin in the analysis plane (y,z). Further, from Eqs. (5.1), one can deduce

$$q=C_q\left[\frac{U(\text{kV})}{I_B^2(\text{mA})}\right]A\left[\frac{Z^2(\text{cm})}{Y(\text{cm})}\right] ,$$
$$E_q(\text{MeV})=C_E\left[\frac{U(\text{kV})}{I_B(\text{mA})}\right]A\left[\frac{Z(\text{cm})}{Y(\text{cm})}\right]^2 . \tag{5.2}$$

I_B is the current producing the static magnetic intensity B. The apparatus constants $C_q=2.8\pm0.3$ and $C_E=1.6\pm0.2$ are fitted for 40-MeV Cu^{7+} and 50-MeV Cu^{8+}-ion beams with $U=47$ kV and $I_B=125$ mA.

The TPS is followed by an ionographic tube (IT) which visualizes the traces (q,E_q) in the analysis plane (20×50 cm). For this purpose, ions impinge on a Au foil. Through secondary emission, electrons are accelerated and amplified through two microchannel plates. Then, they get converted into visible light from a scintillation screen, at the top of an optical fiber device. The ionographic tube works also under a 10^{-7} mbar pressure.

B. Data analysis

The ion beam is probed before and after plasma interaction. Before interaction, the ion beam is pulsed at a frequency $\nu_f=2.5$ MHz and magnetically analyzed to determine E,q,A and mean current intensity I(nA) as well as temporal width. The latter is obtained with a channeltron. After interaction, the heavy-ion beam is analyzed in the TPS and visualized in the IT. Every luminous point receives an E_q,q identification. One also determines the beam fraction Y_q in a given charge state and also the angular dispersion at the plasma exit. Barycentric coordinates of a colored spot yield an average E_q value [see Eq. (5.2)] for the fraction Y_q. The salient information is thus contained in the barycentric coordinates of ion-beam impacts.

In order to implement a standard procedure through Eqs. (5.2), one first determines a C_E upper bound with $E_q\le E$. Then one picks up a recording with a small stopping, dE/dx, pertaining to a weak laser shot, for instance. Moreover, one considers two successive charge states so that [Eq. (5.2)] leads to

$$y_{q+1}-y_q=\left[\frac{AC}{E}\right]^{1/2}\left[\frac{U}{I_B}\right](z_{q+1}-z_q) , \tag{5.3}$$

and

$$C_E = \frac{E}{A}\left[\frac{U}{I_B}\right]^2\left[\frac{\Delta y}{\Delta z}\right]^2 .$$

It thus remains to fix the origin of the analysis plane.

C. Synchronization

As stated above, the ion beam is pulsed with a 2.5-MHz frequency. In principle, it should be possible to launch an ion packet every 400 ns in the expanding plasma. However, the inertia of the data acquisition system (DAS) does not permit that possibility. We have been thus led to use the accelerator in a pulsed regime with a unique ion packet interacting with a single plasma shot. The most conspicuous issue is therefore the timing of that unique ion bunch. We first discuss the synchronization between DAS and the CO_2 laser system.

The imaging system is triggered when the optical fiber device (OFD) emits light under ion impact. The corresponding typical time is ~ 200 nsec, which is the time of flight of ions with $E/A = 0.793$ MeV/amu in the target plasma. The latter duration is a few tens of μs. Those times remain much shorter than video reading time, taken as a reference clock. So, one records information impinging on the OFD for 40 ms after the laser shot, which allows visualizing the ion beam after plasma interaction.

One thus starts initializing the CO_2 laser shot. The shot sequence is secured by a robot charging capacitors of various amplifiers. This step demands several tens of seconds. Then, the robot produces an impulsion received by a pulse generator. This latter finally gives an impulsion directed on the synchronization drawer of the ion-laser system. The signal of the laser charging up is phased with the tandem in order to adjust the shot sequence to the pulsed ion beam.

The synchronization of the laser to the tandem is worked out so that the ion flow in the target chamber is delayed to permit plasma ablation. A basic requirement is therefore the simultaneous detection of the plasma and ion beam in the target chamber. The ion beam is therein localized by inserting a Au foil in its path. Secondary electrons are then collected in a channeltron located 3 cm ahead of the Au foil, and normally to it. During the ion-plasma interaction one makes use simultaneously of an impulse produced by the low-energy deviator or the tandem (see Fig. 10). The plasma is detected through x rays emitted during the heating period. This system thus provides a signal from heated plasma together with a synchronous signal of the bunched ion-beam passage in the target chamber. Those two signals are finally synchronized.

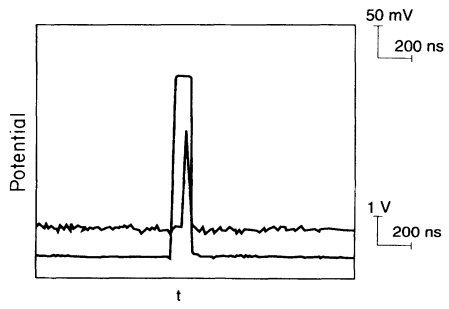

FIG. 10. Oscillogram of the plasma and ion-beam signal in the experimentation chamber. Upper line refers to plasma detected by the X diode. The lower line pertains to the low-energy deviator featuring the ion beam.

VI. PROJECTILE CHARGED DISTRIBUTION IN DENSE PLASMA

Operating the SPQR1 device detailed above (Sec. IV) enables us to study the interaction of Cu^{q+} ions in the $0.6 \le E/A \le 0.8$ MeV/amu energy range, with synchronously fired C and Al plasmas. The corresponding hot targets have an electron temperature $2 \le T_e$ (eV) ≤ 110 and an electron density $10^{17} \le n_e \le 10^{19}$ cm^{-3}. They are typically a few millimeters thick. The ion beam-plasma interaction takes place at 1 mm (core) and 5 mm (corona) above the cold target plate.

A. Ion transmission

We first pay attention to variations of the mean charge

$$\bar{q} = \frac{\sum_q q Y_q}{\sum_q Y_q} , \quad \sum_q Y_q = 1 , \tag{6.1}$$

and relative intensity of four ionization states of the projectile distribution at the plasma exit. These variations are taken first with respect to the interaction time of the ion beam with plasma. The time origin is taken at the plasma ignition. Such an evolution is contrasted to t variations of mean fluence $\overline{n_e l}$ calculated within the expression scheme detailed in Sec. III. To every $(\overline{n_e l}, t)$ point, there is a T_e value measured by charge collectors (Sec. IV). First, we pay attention to ion interaction with the core, the dense part of the ablated plasma. The beam center then flies 1 mm above the laser focal spot (Figs. 11 and 13). Next, we consider the interaction with the plasma corona 5 mm above the target plate, as shown in Fig. 12.

In the dense region (Fig. 11), $\bar{q}$ variations for a Cu-Al interaction at the plasma exit are correlated to $\overline{n_e l}$. $\bar{q}$ decay consists of two negative slopes, with a change taking place at $t \sim 20$ μsec. Beyond that value, $\bar{q}$ converges to the inertial charge 9. $\overline{n_e l}$ values are given in Fig. 11(a) by the earliest dense plasma phase. When $\overline{n_e l} \ge 10^{16}$ cm^{-3}, $q \to 10$, and, when larger than 10^{17} cm^3, it goes up to 11 and 12. Simultaneously, $\bar{q}$ increases steadily up to 11.7 ($\overline{n_e l} \sim 2.10^{18}$ cm^{-2}). Figure 12 displays similar trends for a coronal plasma with an ion beam 5 mm above the target plate. Now, one no longer witnesses a correlation between $\overline{n_e l}(t)$ and $\bar{q}(t)$. Although our modeling predicts a decaying $\overline{n_e l}$, $\bar{q}$ steadily increases [Fig. 12(b)] up to $t = 10$ μsec and reaches a plateau value $q_{\max} \simeq 12$. It peaks at 13 before a swift decay. It should be appreciated that in the plasma center [Fig. 11(b)] $\bar{q}$ decreases steadily, while in the corona [Fig. 12(b)] it increases most of the time. Nonetheless, in both cases $\bar{q}$ greater than or equal to the initial value after 65 nsec with $\bar{q} \sim 11.5$. In the corona re-

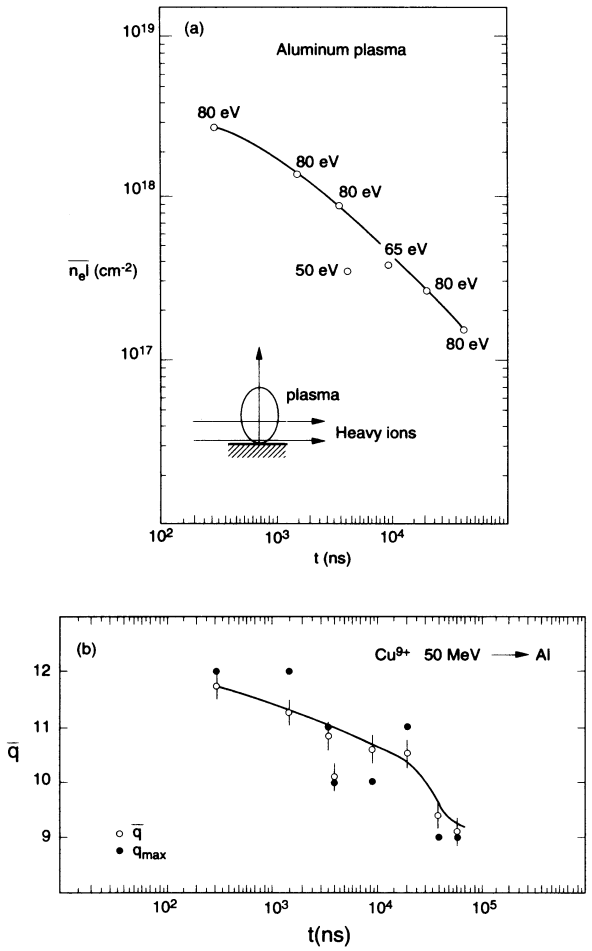

FIG. 11. (a) Mean linear electron density in expanding Al in plasma at 1 mm from the target plate. (b) Average projectile charge state $\bar{q}$ in terms of interaction time in an Al plasma for a 50-MeV Cu^{9+} ion beam at the 1-mm target plate.

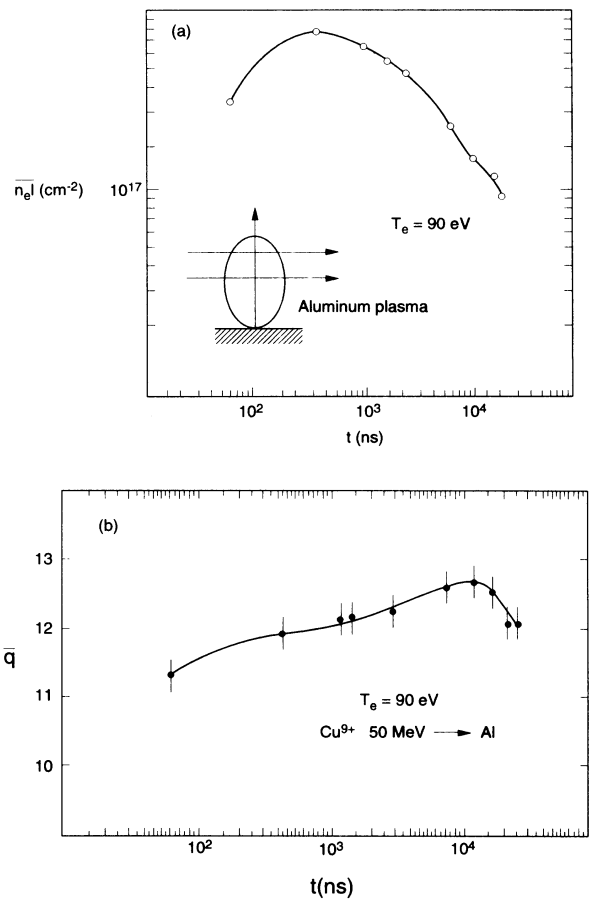

FIG. 12. (a) and (b) Same caption as in Fig. 10 for a beam at the 5-mm target plate.

gime, one observes $\bar{q}$ approximately equal to the constant over a large $n_e l$ range, which emphasizes an equilibrium charge.

These behaviors highlight a global agreement between modeling and measurements. Figure 13 displays $\bar{q}$ and Y_q variations of Cu^{9+} ions in an Al plasma. The four selected charge states enclose the maximum of the Y_q distribution. This behavior documents a nearly instantaneous ionization of energetic ion projectiles in a hot target with moderate atomic number Z. It confirms earlier numerical predictions. Figure 13 features a marked Y_q decay for a fluence $\sim 10^{16}$ e cm^{-2}. All in all, one observes, as expected, a rapid ionization stabilized on a plateau value.

B. Charge distribution at fixed N_e and T_e

Now, we turn to a thorough study of distributions of projectiles charge states at the exit of C and Al plasmas. The observation of a complete Y_q distribution is obtained through a series of laser shots with fixed parameters (interaction time, laser power, etc.). Resulting Y_q distributions are parametrized by experimental conditions: measured T_e, plasma temperature T_{inter}, and fluence $n_e l$ at time Δt after laser ignition. Moreover, the quantities

$$d^2 = \sum_q (q - \bar{q})^2 Y_q \ ,$$

width

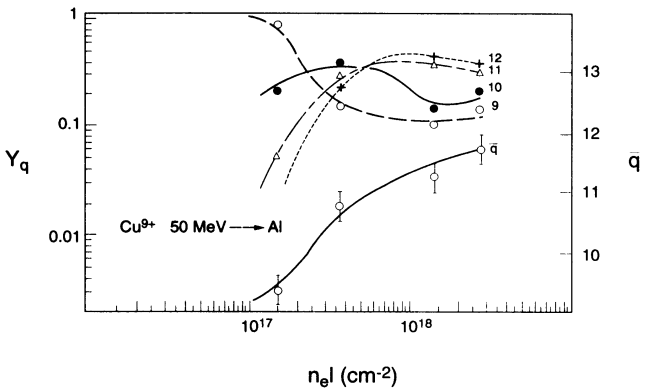

FIG. 13. Evolution of $\bar{q}$ and Y_q of four charges around the maximum distribution, in terms of the mean electron linear density. Cu^{9+} ions flow 1 mm above the target plate in an Al plasma.

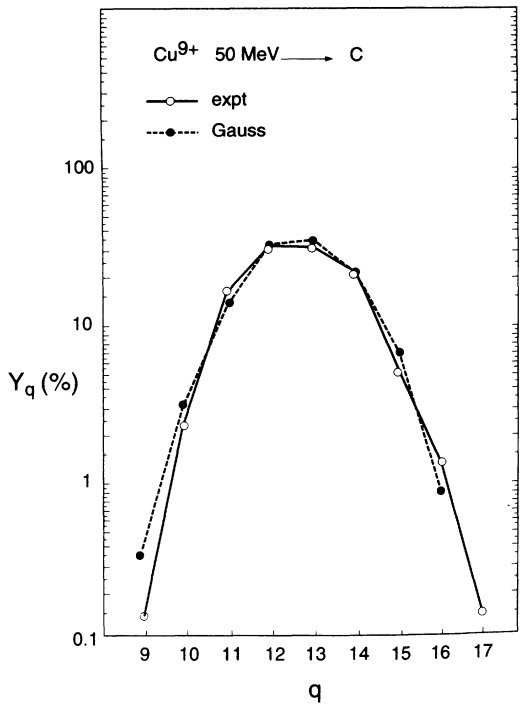

FIG. 14. Y_q distribution in a C target (Table I) with a Gaussian fit.

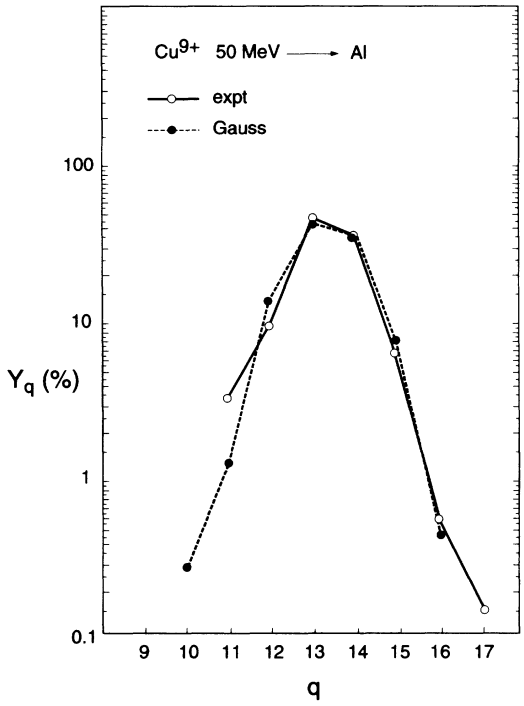

FIG. 15. Y_q distribution in an Al target (Table II) with a Gaussian fit.

TABLE I. Experimental parameters of the Y_q distribution featured in Fig. 14.

Plasma			Heavy ions: $\sum Y_Q = 100$					
T_e (eV)	T_{int} (eV)	$\overline{n_e l}$ (cm^{-2})	$\bar{q}$	q_{max}	$q^{\bar{2}}$	Width d	Asymmetry s	$q^{\bar{2}}_G$
			Interaction at 1 mm					
70	5	8×10^{17}	12.7	13	162.1	1.2	0.12	162.8

TABLE II. Experimental parameters of the Y_q distribution featured in Fig. 15.

Plasma			Heavy ions: $\sum Y_Q = 100$					
T_e (eV)	T_{int} (eV)	$\overline{n_e l}$ (cm^{-2})	$\bar{q}$	q_{max}	$q^{\bar{2}}$	Width d	Asymmetry s	$q^{\bar{2}}_G$
			Interaction at 5 mm					
90	2	5×10^{17}	13.3	13	178.6	0.9	−0.13	178.7

TABLE III. Experimental parameters of the Y_q distribution featured in Fig. 16.

Plasma			Heavy ions: $\sum Y_Q = 100$					
T_e (eV)	T_{int} (eV)	$\overline{n_e l}$ (cm^{-2})	$\bar{q}$	q_{max}	$q^{\bar{2}}$	Width d	Asymmetry s	$q^{\bar{2}}_G$
			Interaction at 1 mm					
60	60	1.5×10^{18}	13.9	14	194.5	1.5	0.31	195.5

TABLE IV. Experimental parameters of the Y_q distribution featured in Fig. 17.

Plasma			Heavy ions: $\sum Y_Q = 85$					
T_e (eV)	T_{int} (eV)	$\overline{n_e l}$ (cm^{-2})	$\bar{q}$	q_{max}	$q^{\bar{2}}$	Width d	Asymmetry s	$q^{\bar{2}}_G$
			Interaction at 1 mm					
80	80	2×10^{18}	12.9	13	168.2	1.1	0.35	168.1

$$\overline{q^2}=\bar{q}^2+d^2 , \tag{6.2}$$

average quadratic charge

$$s=\sum_q (q-\bar{q})^3 Y_q d^{-3} ,$$

asymmetry, and q_{max} are also tabulated.

On captions featuring experimental Y_q data, one also superimposes a Gaussian distribution

$$Y_q=(2\pi d^2)^{-1/2}\exp[-(q-\bar{q})^2/2d^2] , \tag{6.3}$$

with the same $\bar{q}$ and d as the experimental distribution. Usually, $\bar{q}$ is not an integer. However, $\bar{q}=q_{max}$ for symmetric cases. So, let us first consider a C target with initial temperature $T_e=70$ eV and $T_{inter}=5$ eV (cf. Table I and Fig. 14). The ion beam penetrates the dense plasma core 1 mm above the target plate with a time delay $\Delta t=200$ nsec. Then, observed Y_q distribution is very close to a Gaussian for $q\simeq\bar{q}$. Discrepancy slightly increases with $|q-\bar{q}|$.

The Al target with initial $T_e=90$ eV is displayed in Fig. 15 (see also Table II). Then $t=2.1$ μsec. Now, the ion beam is probing the plasma corona at 5 mm from the cold target plate. T_{inter} and $\overline{n_e l}$ are consequently smaller than in the previous case. Y_q distribution is again well fitted by a Gaussian which shows a bit of narrowing with respect to the experiment.

The negative s value signals the largest asymmetry for $q\geq\bar{q}$. In Tables I and II, T_e and $\overline{n_e l}$ feature rather similar plasma conditions, which shows that the plasma ion density is largest for the smallest Z atomic number, when

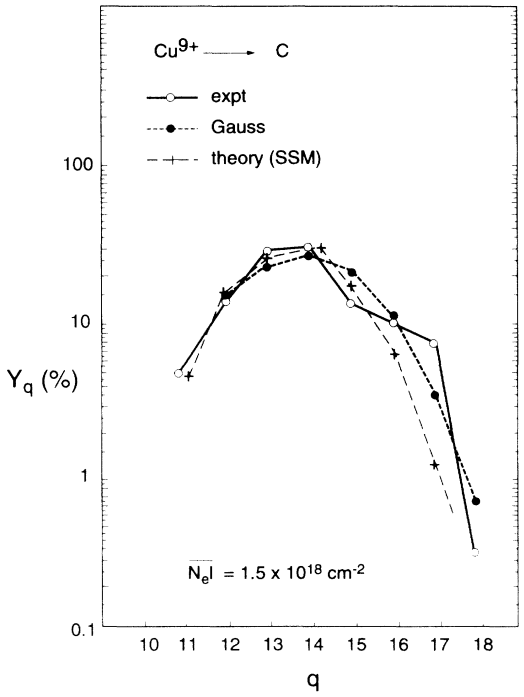

FIG. 16. Y_q distribution in a C target (Table III) with a Gaussian fit. The SSM theoretical result is obtained for a density $n_{C^{5+}}=3\times10^{17}$ cm^{-3}.

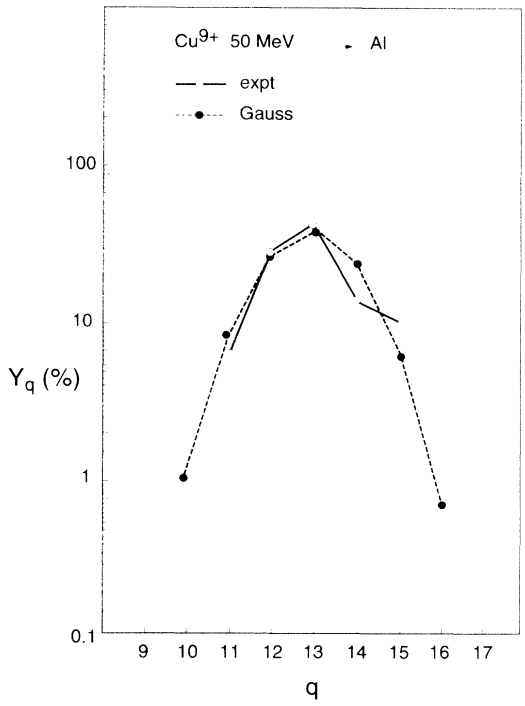

FIG. 17. Y_q distribution in an Al target (Table IV) with a Gaussian fit.

$\overline{n_e l}$ is kept constant. As a consequence, the charge-exchange recombination is expected to be larger in Al than in C plasma, which yields smaller projectile ionization in Al than in C. These expectations indeed appear documented in Figs. 16 and 17 (see, respectively, Tables III and IV) for an incoming Cu^{9+} beam at a 1-mm target

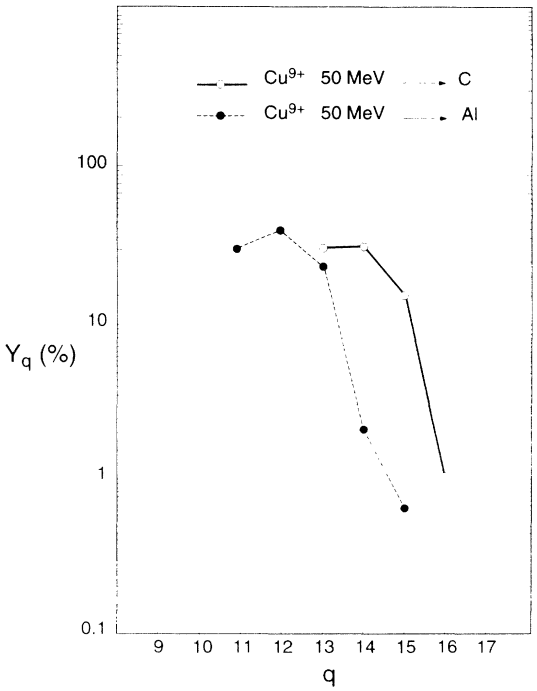

FIG. 18. Comparison of Y_q distributions in C and Al targets with $T_e=80$ eV and $\overline{n_e l}=4\times10^{18}$ cm^{-2}.

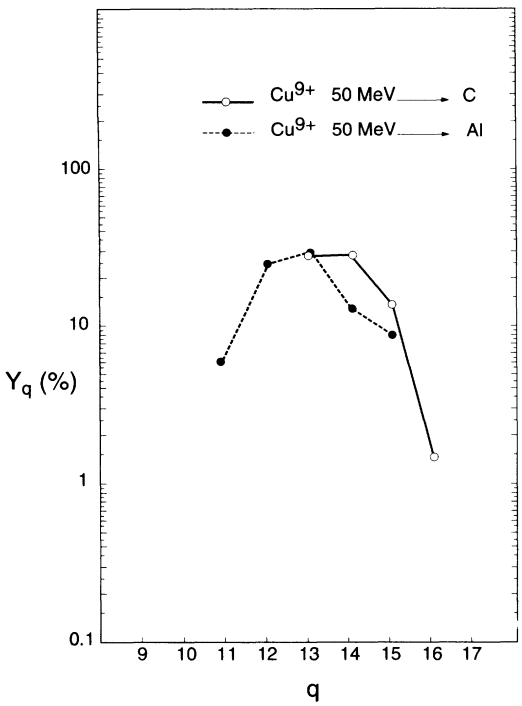

FIG. 19. Comparison of Y_q distribution in C ($T_e=110$ eV, $\overline{n_e l}=7\times10^{18}$ cm^{-2}) and Al ($T_e=100$ eV, $\overline{n_{el}}=10^{19}$ cm^{-2}).

plate. Figure 16 pertains to a C target with $T_e=60$ eV and $\Delta t=150$ ns (Table III). The theoretical SSM curve is obtained for $n_{C^{5+}}=3.10^{17}$ cm^{-3}. Here, $s\sim0.3$ accounts for a moderately successful fit with a Gaussian distribution. The same remark applies to the Al case (Fig. 17). Then, it appears useful to contrast Tables I and III, featuring a nearly equal initial T_e value. Only $\overline{n_e l}$ is notably different. The largest $\overline{n_e l}$ (Table III, C) also gets larger values for the other parameters, which include $\bar{q}$ and $q_{\max}$. Then, one notices that for a lower bound-electron density, recombination induced by charge exchange is also smaller, which increases projectile ionization. It should be stressed that in Fig. 17 (Table IV) the statistics are incomplete, with $\sum_q Y_q=85$ instead of 100. It is also gratifying that a theoretical Y_q distribution based on the SSM model (Sec. II) fits pretty well the measured one given in Fig. 16.

The high-q part of the Y_q distribution is compared in Fig. 18 for incoming Cu^{9+} ions interacting with different targets featuring identical plasma conditions ($\overline{n_e l}, T_e$). As expected from previous discussions, one observes a $\bar{q}$ shift toward higher q values for a small Z (carbon) plasma. Again, this result accounts for an enhanced bound-bound recombination in Al. Figure 19, with very similar but not identical plasma conditions, confirms a similar trend.

C. Width and asymmetry

Width d and asymmetry s data are now reported in Fig. 20, in terms of $\overline{n_e l}$ variations, at fixed T_e for a 50-MeV Cu^{9+} ion stopped in a hot Al target. Conditions

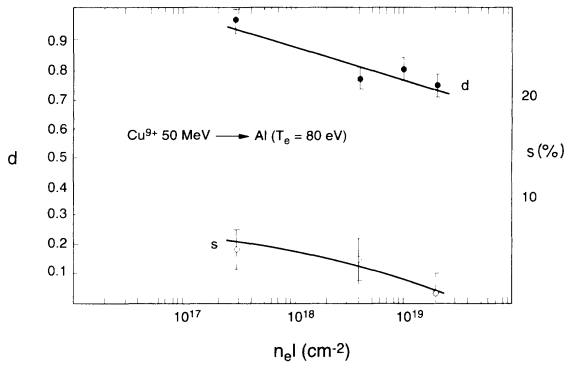

FIG. 20. Width d and asymmetry s in terms of $\overline{n_{el}}$ for an Al target at 80 eV.

and parameters are those already encountered in Fig. 18. One observes that d and s decrease when $\overline{n_e l}$ increases. For all $\overline{n_e l}$ one gets $d<1$ and $S\geq0.05$. These d and s values are systematically below their cold (gas or solid) matter equivalent (same $\overline{n_e l}$).

VII. ION STOPPING IN DENSE PLASMA

As far as stopping is concerned, the SSM theory developed previously in Sec. II A provides an adequate framework for analysis that is analogous to the one already used for ion-stopping measurements in dense and fully ionized hydrogen (SPQR2) projects). First, we consider the stopping of 50-MeV $^{63}_{29}Cu^{9+}$ ion s in C and Al plasmas, in terms of linear electron density, at fixed T_e. The measured mean ion exit energy

$$\bar{E}=\frac{\sum_q E_q Y_q}{\sum_q Y_q}\ ,\quad \sum_q Y_q=100$$

has to be compared to the corresponding SSM calculated value

$$\bar{E}_{\text{calc}}=E_f-\Delta\bar{E}\ ,$$

$$\Delta\bar{E}=\text{ mean theoretical energy loss (2.7)}\ . \qquad (7.1)$$

In Fig. 21(a), $\bar{E}$ and $\bar{E}_{\text{calc}}$ are compared to an 80-eV Al plasma with an electron temperature $T_e=80$ eV. The corresponding $\overline{n_e l}$ ranges between 10^{17} and 10^{19} cm^{-2}. As expected, measured $\Delta\bar{E}$ increases with the average quadratic charge $\bar{Z}_f^2=\overline{q^2}$. In Fig. 21(b), the target is a carbon plasma with $10^{18}\leq\overline{n_e l}\leq8\times10^{18}$ cm^{-2} and $T_e=60$ eV. Measured $\Delta\bar{E}$ increases with $\bar{Z}_f^2$ and also with $\overline{n_e l}$, which confirms the basic SSM trends for a nonhydrogenic target. A very significant result is that fixed for T_e and n_e; a lower Z target is likely to produce a larger energy loss. This feature appears well documented for $\bar{E}$ in Figs. 21(a) and 21(b), which exhibits a larger stopping in a C plasma. Actually, $\bar{E}=40$ MeV is reached as soon as $\overline{n_e l}=8.10^{18}$ cm^{-2} for C, whereas the same $\bar{E}$ value demands $\overline{n_e l}=2.10^{19}$ cm^{-2} for Al.

Figures 21(a)–21(c) demonstrate a good agreement between calculated and measured average energy losses.

However, theory systematically appears slightly above experiment. Nevertheless, the largest discrepancies are only a few percent.

It should be noted that in Figs. 21(a) and 21(b), the average target ionization is around 5 for C and 8 for Al. So one deduces $n_e\bar{l}$ in both cases. One witnesses an enhanced stopping by a factor 5 in C relative to that in a cold target with the same $n_i\bar{l}$. In Al, the enhancement is 3.2.

In Figs. 21(a)–21(c) curves are given just for guiding the eyes. These results are the first confirmation of the EPS effect in nonhydrogenic hot targets at several tens of eV.

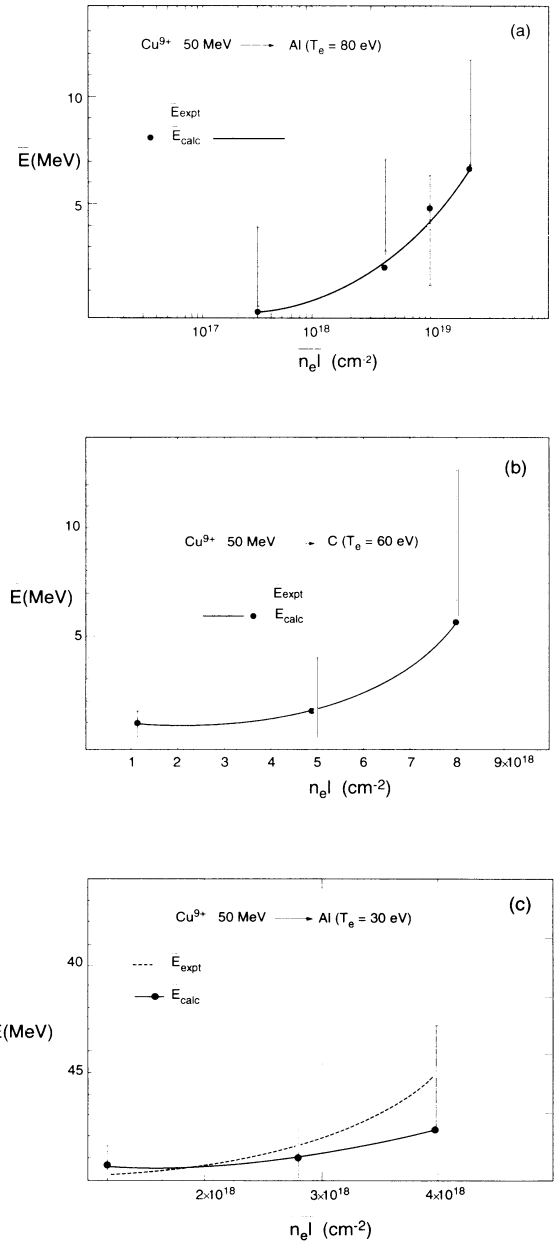

FIG. 21. Measured mean energy $\bar{E}_{\text{expt}}$ of Cu ions with 50 MeV initial energy compared to SSM $\bar{E}_{\text{calc}}$ (7.1): (a) Al target ($T_e=80$ eV); (b) C target ($T_e=60$ eV); (c) Al target ($T_e=30$ eV).

VIII. CONCLUSION AND SUMMARY

The experimental investigation reported here concerns essentially the stopping and charge-state distribution of 50-MeV Cu^{9+} ions at (0.7–0.8) MeV/amu interacting with a laser-ablated C or Al plasma. The novelty of this work consists in synchronizing plasma production and diagnostics with inflight beam spectrometry. The space-time expansion of the laser-ablated target is modeled by taking initial laser irradiation and measured velocities of collected plasma charges as limit conditions.

We have first demonstrated that mean ionization of an ion beam in hot C and Al targets with T_e on the order of a few tens of eV and $n_e\bar{l}\sim 10^{18}e$ cm^{-2} is larger than in the equivalent cold gas. In the present plasma case, the equilibrium charge is not reached, even though the plasma linear densities correspond to thicknesses of the cold target that are sufficient to get the equilibrium projectile charge.

These findings highlight the importance of bound-state electrons in the target plasmas. These electrons are indeed responsible for the important recombination of projectile ions through exchange with target bound states. For fixed T_e and n_e values, it is the target with the smallest Z which produces the highest projectile ionization. Post ionization at the plasma exit looks negligible. Ion charge distributions appear nearly Gaussian. Their widths are smaller than those pertaining to equivalent cold targets with the same $n_e\bar{l}$. Their asymmetries are also of the same order of the cold gas equivalent.

Distributions obtained in Al plasma ($T_e=80$ eV) demonstrate a decay of width and asymmetry when $n_e\bar{l}$ decreases. Ion stopping gets enhanced by a factor of 5 in a C plasma ($T_e=60$ eV) and by a factor of 3.2 in Al plasma ($T_e=80$ eV) when compared to their cold target homologous with the same $n_e\bar{l}$. These results are of obvious interest in asserting the feasibility of inertial confinement fusion driven by intense ion beams.

ACKNOWLEDGMENT

The Laboratoire de Physique des Gaz et Plasmas is associé au CNRS.

APPENDIX A: ELECTRON DENSITY PROFILE AT THE END OF LASER PULSE

Laser light is essentially absorbed in the vicinity of critical density

$$\rho_{\text{cr}}=\frac{m_e\epsilon_0\omega_L^2}{e^2}\frac{m_i}{Z}\ . \tag{A1}$$

One considers a pointlike absorption at $\rho=\rho_{\text{cr}}$.

Restricting to $\rho<\rho_{\text{cr}}$, the plasma remains transparent, whereas for $\rho=\rho_{\text{cr}}$, the light flux transforms into heat flux. We can therefore write, in spherical coordinates, the usual [14,15] hydrodynamic equations pertaining to charge, momentum, and energy conservation.

Restricting ourselves to the first step with a stationary flow, this system may be integrated through

$$\frac{d(\rho V_r)}{\rho V_r}=\frac{2dr}{r}\ ,\quad \text{with } \rho V_r r^2=\text{const}\ , \tag{A2}$$

for the continuity equation,

$$\frac{d}{dr}(p+\rho V_r^2)=-2\rho V_r^2$$

for the momentum equation, and also

$$\rho V_r r^2\left[\varepsilon+\frac{V_r^2}{Z}\frac{p}{\rho}\right]-r^2\chi_0 T_e^{5/2}\frac{\partial T_e}{\partial r}=\begin{cases}Q_L\ , & r>r_{\rm cr}\\ 0\ , & r<r_{\rm cr}\end{cases}$$

for the energy conservation. Q_L is the flux of electromagnetic flux. $r_{\rm cr}$ is the radius such that $\rho=\rho_{\rm cr}$. The solution of Eqs. (A2), as worked out by Afanas'ev [14], makes use of a reference Jouget point r_S with expansion velocity equal to local sound velocity. So, one writes the reference velocity as

$$(\bar{Z}+1)k_B T_S=m_1 V_S^2\ .$$

The initial plasma is taken as a sphere with a radius equal to that of the laser focal spot r_0. In practice, one looks for solutions fulfilling $T_e(r\gg r_0)=T_{\max}$, the ion temperature measured by charge collectors discussed in the main text. At the other extreme, one assumes that T_e and the expansion velocity vanish at the target spot, so that

$$T(r_0)=0\ ,\quad V_r(r_0)=0\ ,\quad \rho(e_{\rm cr})=\rho_{\rm cr}\ . \tag{A3}$$

The solution with limit conditions (A3) is worked out through a dimensionless parameter

$$\gamma_0=\frac{\chi_0^{3/4}Q_L}{\rho_{\rm cr}^{7/4}r_0^{11/4}}\left[\frac{m_i}{Z}\right]^{21/8}\ .$$

When $r_0\le r\le r_{\rm cr}$, one gets

$$\begin{aligned}T(r)&=T_S\left[1+15.4\left[1-\frac{1.2r_0}{r}\right]+\frac{7.7r_0}{r}\log_{10}\left[1-\frac{1.2r_0}{r}\right]\right]^{2/7}\ ,\\ n_e(r)&=n_S\left[1-6.4\log_{10}\left[\frac{1.2r_0}{r}\right]\right]^{-1/2}\ .\end{aligned} \tag{A4}$$

In the domain $r>r_{\rm cr}$, one obtains

$$T(r>r_{\rm cr})=T_{\max}\left[1+\frac{(T_{\rm cr}-T_{\max})}{T_{\max}}\left[\frac{r_{\rm cr}}{r}\right]^{4/3}\right]\ ,$$

$$n_e(r>r_{\rm cr})=n_S\left[11-6.5\log_{10}\left[\frac{\gamma_0^{2/7}}{4}\right]-\frac{3.2\gamma_0^{8/21}\left[\frac{1.2r_0}{r}\right]^{4/3}}{\left[1+6.4\log_{10}\left[\frac{\gamma_0^{2.7}}{4}\right]\right]^{1/2}}\right]^{-1/2}\ , \tag{A5}$$

where $n_S=0.17n_{e\rm cr}\gamma_0^{4/7}\left[\frac{1.2r_0}{r}\right]^2$.

APPENDIX B: SPACE-TIME EVOLUTION OF N_e AND T_e

In order to determine the space-time profiles for n_e and T_e, one considers a system with a homogeneous expansion at every fluid point. The Kidder [15] Lagrangian formalism is well suited to this problem. It makes use of the particle's position at given time $t_0=\tau_L$, end of laser pulse, with vector $\mathbf{P}_{t0}$ (components x_1,x_2,x_3). At time t, a particle position is $\mathbf{P}=\mathbf{P}(\mathbf{P}_{t0},t)$ and the velocity of fluid around $\mathbf{P}$ at t is $\mathbf{V}-\partial\mathbf{P}/\partial t$. Then, if one considers a given volume element at the initial time, it becomes $d\mathbf{r}=h^3(t)d\mathbf{r}_0$ at a future time, where $h(t)$ is dimensionless and t-dependent only.

In a one-dimensional situation, the space component behaves as $r(r_0,t)=h(t)r_0$ and the velocity as $v_r(r_0,t)=(\partial/r/\partial t)=r_0(\partial h/\partial t)$.

The t dependence may be given a Bobin-Reisse expression [19]

$$h(t)=\left[1+\left[\frac{t-\tau_L}{\tau_1}\right]^2\right]^{1/2}\ , \tag{B1}$$

which models the spherical expansion through

$$T_e(r_0,t)=\frac{T_0}{1+\left[\frac{t-\tau_L}{\tau_L}\right]^2}\ , \tag{B2}$$

$$n_e(r_0,t)=\frac{n_0}{\left[1+\left[\frac{t-\tau_L}{\tau_L}\right]^2\right]^{3/2}}\ . \tag{B3}$$

[1] R. O. Bangerter, Fus. Technol. **13**, 348 (1988).
[2] F. C. Young, D. Mosher, S. J. Stephanakis, Shyke A. Goldstein, and T. A. Mehlhorn, Phys. Rev. Lett. **49**, 549 (1982).
[3] C. Deutsch, Ann. Phys. (Paris) **11**, 1 (1986); Laser Part. Beam **2**, 449 (1984).
[4] R. Deicas, CEN Bruyères-le-Chatel, Report No. CEA-R-5119, 1981 (unpublished).
[5] C. Deutsch, G. Maynard, R. Bimbot, D. Gardès, S. Della-Negra, M. Dumail, B. Kubica, A. Richard, M. F. Rivet, A. Servajean, C. Fleurier, A. Sanba, D. H. H. Hoffmann, K. Weyrich, and H. Wahl, Nucl. Instrum. Methods A **278**, 38 (1989); C. Deutsch, Comments At. Mol. Phys. **23**, 111 (1989).
[6] J. Meyer-ter-Vehn, S. Witkowski, R. Bock, D. H. H. Hoffmann, I. Hoffmann, R. W. Müller, R. Arnold, and P.

Mulser, Phys. Fluids, B **2**, 1313 (1990); D. Gardès, R. Bimbot, S. Della Negra, M. Dumail, B. Kubica, A. Richard, M. F. Rivet, A. Servajean, C. Fleurier, A. Sanba, C. Deutsch, G. Maynard, D. H. H. Hoffmann, K. Weyrich, and H. Wahl, Europhys. Lett. **8**, 701 (1988); D. H. H. Hoffmann, K. Weyrich, H. Wahl, Th. Peter, J. Meyer-Ter-Vehn, J. Jacoby, R. Bimbot, D. Gardès, M. F. Rivet, M. Dumail, C. Fleurier, A. Sanba, C. Deutsch, G. Maynard, R. Noll, R. Hass, R. Arnold, and S. Maurmann, Z. Phys. A **30**, 339 (1988).

[7] D. Gardès, A. Servajean, B. Kubica, C. Fleurier, D. Hong, C. Deutsch, and G. Maynard, Phys. Rev. A **46**, 5101 (1992).

[8] D. W. Hewett, W. L. Kruer, and R. O. Bangerter, Nucl. Fus. **31**, 431 (1991); C. Deutsch, P. Fromy, X. Garbet, and G. Maynard, Fus. Technol. **13**, 362 (1988).

[9] E. Nardi and Z. Zinamon, Phys. Rev. Lett. **49**, 1251 (1982); M. Chen, Phys. Rev. A **44**, 4215 (1991); D. Bailey, Y. T. Lee, and R. M. More, J. Phys. (Paris) Colloq. **44**, C8-149 (1983); G. I. Bell, Phys. Rev. **90**, 548 (1953).

[10] For a recent discussion, see G. Maynard and C. Deutsch, Phys. Scr. **48**, 471 (1993); G. Maynard and C. Deutsch, J. Phys. (Paris) Colloq. **49**, C7-151 (1988).

[11] J. M. Guihaumé, R. Deicas, M. A. Beuve, J. F. Glicenstein, J. P. Laget, C. Moreau, J. P. Mosnier, M. Renaud, R. Barchewitz, and M. Cukier, in *Heavy Ion Inertial Fusion, Washington, D.C., 1987,* Proceedings of the International Symposium on Heavy Ion Fusion, edited by Martin Reiser, Terry Godlove, and Roger Bangerster, AIP Conf. Proc. No. **152** (AIP, New York, 1986), p. 360.

[12] D. Schirmann, P. Grelot, M. Rabeau, and G. Tonon, CEN Limeil, Report No. CEA-R-4299, 1972 (unpublished).

[13] J. W. Shearer and W. S. Barners, Laser Interact. Relat. Plasma Phenom. **1**, 307 (1971).

[14] Yu. V. Afanas'ev, E. G. Gamalii, O. N. Krokhin, and V. E. Rosanov, Zh. Eksp. Teor. Fiz. **71**, 594 (1976) [Sov. Phys. JETP **44**, 311 (1976)].

[15] R. E. Kidder, Nucl. Fusion, **14**, 53 (1974).

[16] R. Deicas, J. Bardy, M. A. Beuve, J. P. Aget, A. Menier, M. Renaud, J. Phys. (Paris) Colloq. **44**, C8-179 (1983).

[17] J. M. Guihaumé, R. Deicas, M. A. Beuve, and S. Joly, J. Phys. (Paris) Colloq. **49**, C7-173 (1988); E. Nardi and Z. Zinamon, Phys. Rev. Lett. **49**, 1251 (1982).

[18] C. Couillaud, Ph.D. thesis, Université Paris XI, 1992 (unpublished).

[19] J. L. Bobin and J. M. Reisse, Rev. Phys. Appl. **14**, 497 (1976).